FILAMENTS, BUBBLES, AND WEAK SHOCKS IN THE GASEOUS ATMOSPHERE OF M87

W. Forman,[1] C. Jones,[1] E. Churazov,[2,3] M. Markevitch,[1] P. Nulsen,[1] A. Vikhlinin,[1,2] M. Begelman,[4]
H. Böhringer,[5] J. Eilek,[6] S. Heinz,[7] R. Kraft,[1] F. Owen,[8] and M. Pahre[1]

ABSTRACT

We present the first results from a 500 ks *Chandra* ACIS-I observation of M87. At soft energies (0.5–1.0 keV), we detect filamentary structures associated with the eastern and southwestern X-ray and radio arms. Many filaments are spatially resolved with widths of ∼300 pc. This filamentary structure is particularly striking in the eastern arm, where we suggest the filaments are outer edges of a series of plasma-filled, buoyant bubbles whose ages differ by ∼6×10^6 yr. These X-ray structures may be influenced by magnetic filamentation. At hard energies (3.5–7.5 keV), we detect a nearly circular ring of outer radius $2.8'$ (13 kpc), which provides an unambiguous signature of a weak shock, driven by an outburst from the supermassive black hole (SMBH). The density rise in the shock is $\rho_{\rm shock}/\rho_0 \approx$ 1.3 (Mach number, $M \approx 1.2$). The observed spectral hardening in the ring corresponds to a temperature rise $T_{\rm shock}/T_0 \approx 1.2$, or $M \approx 1.2$, in agreement with the Mach number derived independently from the gas density. Thus, for the first time, we detect gas temperature and density jumps associated with a classical shock in the atmosphere around a SMBH. We also detect two additional surface brightness edges and pressure enhancements at radii of ∼$0.6'$ and ∼$1'$. The ∼$0.6'$ feature may be overpressurized thermal gas surrounding the relativistic plasma in the radio cocoon, the "piston," produced by the current episode of AGN activity. The overpressurized gas is surrounded by a cool gas shell. The ∼$1'$ feature may be an additional weak shock from a secondary outburst. In an earlier episode, the piston was responsible for driving the $2.8'$ shock.

Subject headings: galaxies: active — galaxies: individual (M87, NGC 4486) — X-rays: galaxies

1. INTRODUCTION

M87 (NGC 4486), the dominant central galaxy in the Virgo Cluster, hosts a 3.2×10^9 $M_\odot$ supermassive black hole (SMBH; Harms et al. 1994; Ford et al. 1994; Macchetto et al. 1997) and its well-studied jet (e.g., Sparks et al. 1996; Perlman et al. 2001; Marshall et al. 2002; Harris et al. 2003). On larger scales M87 has been the subject of detailed radio observations showing remarkable structures on scales up to 40 kpc (Owen et al. 2000; see also Hines et al. 1989). In soft X-rays, M87 is the second brightest extragalactic source (after the Perseus Cluster), and the emission is dominated by thermal radiation from its ∼2 keV gaseous atmosphere (e.g., Gorenstein et al. 1977; Fabricant & Gorenstein 1983; Böhringer et al. 2001; Matsushita et al. 2002; Belsole et al. 2001; Molendi 2002).

M87 is a classic example of a "cooling flow" cluster (e.g., Fabian 1994). *XMM-Newton* and *Chandra* observations (e.g., David et al. 2001; Peterson et al. 2004 and references therein) limit the amount of cooling gas in cluster cores to 10%–20% of that predicted by the standard cooling flow model and suggest that the average core temperature does not fall below ∼30% of the gas temperature at large radii. The dramatic reduction in the amount of cooling gas, compared to the standard model, requires a considerable energy supply to compensate for the observed radiative losses. Thus, instead of seeking the repository of

cold gas, we are now seeking the energy source to (re)heat the radiating gas.

Suggestions for heating include thermal conduction (e.g., Tucker & Rosner 1983; Bertschinger & Meiksin 1986; Gaetz 1989; David et al. 1992; Zakamska & Narayan 2003; Voigt & Fabian 2004) and cluster mergers (e.g., Fujita et al. 2004; but see Böhringer et al. 2004). One of the most promising heating mechanisms has been SMBH outbursts. Strong shocks are rare, and most heating probably arises from less violent mechanisms to transfer active galactic nucleus (AGN) mechanical power into heating the thermal plasma. Buoyant bubbles, inflated by SMBH activity, were first modeled for M87 by Churazov et al. (2001; see also Reynolds et al. 2001; Kaiser & Binney 2003; DeYoung 2003). These bubbles can be a significant energy source for the cooling gas and can explain much of the radio and X-ray morphology (Churazov et al. 2001, 2002; Quilis et al. 2001; Brüggen et al. 2002). The energy of jets and buoyant bubbles can be transferred to the radiating gas by shocks, gravity waves, or turbulence (e.g., Churazov et al. 2002; Ruszkowski et al. 2004a, 2004b; Begelman 2004; Omma et al. 2004; Roychowdhury et al. 2004, 2005; Heinz & Churazov 2005; Mathews et al. 2006; Binney et al. 2007). From deep *Chandra* observations of the Perseus Cluster, Fabian et al. (2006) showed that pressure ripples could balance radiative cooling in the Perseus core, if the viscosity is high. Dunn et al. (2005) showed that buoyant bubbles may be a significant heat source in 70% of a sample of cooling core clusters (see also Birzan et al. 2004).

As the nearest cooling core cluster with an active nucleus, M87 is an ideal system for studying the energy input from the AGN to the hot, cooling gas. The first suggestion of structure in the gaseous halo of M87 and its possible relation to the radio structure was made by Feigelson et al. (1987). Subsequently, with ever-improving angular resolution, the relationship has been explored in more detail (Böhringer et al. 1995; Churazov et al.

[1] Smithsonian Astrophysical Observatory, Harvard-Smithsonian Center for Astrophysics, Cambridge, MA 02138; wforman@gmail.com.
[2] Space Research Institute (IKI), Moscow 117810, Russia.
[3] Max-Planck-Institut für Astrophysik, 85740 Garching, Germany.
[4] Joint Institute for Laboratory Astrophysics (JILA), University of Colorado, Boulder, CO 80309.
[5] MPI für Extraterrestrischephysik, 85748 Garching, Germany.
[6] New Mexico Tech, Socorro, NM 87801.
[7] University of Wisconsin, Madison, WI 53706.
[8] National Radio Astronomy Observatory, Socorro, NM 87801.

2001; Belsole et al. 2001). In an earlier 40 ks *Chandra* observation, Young et al. (2002) reported X-ray cavities and edges in the surface brightness profile. In a longer (~100 ks) *Chandra* observation, Forman et al. (2005) suggested that the edges or rings of enhanced emission at 13 and 17 kpc were likely shock fronts associated with AGN outbursts that began $(1-2) \times 10^7$ yr ago. From these same observations, Jordan et al. (2004) identified a population of ~150 low-mass X-ray binaries (LMXBs), 40% of which are associated with globular clusters.

We report here on the 500 ks observation of M87 with the *Chandra Observatory*. We focus on two major results:

1. The soft emission (0.5–1.0 keV) from M87, especially in the eastern and southwestern arms, forms a web of *resolved* filamentary structures (broader in extent than a point source) of width ~300 pc (see Fig. 2). These features, especially those seen in the eastern arm, may arise from a series of buoyant bubbles at different heights in the atmosphere and different stages of evolution.

2. The hard emission (3.5–7.5 keV) shows a ring of emission (see Fig. 7) that is nearly circular with an outer radius ranging from 2.5′ to 2.85′ (11.6–13.3 kpc). This ring of hard emission provides an unambiguous signature of a weak shock. Hardness ratios (deprojected) show that the gas temperature in the ring rises from ~2.0 to ~2.4 keV, implying a Mach number of $M \sim 1.2$ (shock velocity $v = 880$ km s^{-1} for a 2 keV thermal gas). At the shock, the density jump is 1.33, which yields a Mach number of 1.22, consistent with that derived from the temperature jump. The age of the outburst that gave rise to the shock must be approximately the radius of the shock divided by the shock velocity, $t_{\text{outburst}} \lesssim R_{\text{shock}}/v_{\text{shock}} = 14$ Myr.

In addition to these results, the *Chandra* image provides a wealth of information on structures with scales from the jet to large-scale cavities. We will discuss these other features in more detail in future papers and focus here on the two new results from the soft- and hard-band images from the deep observation.

2. OBSERVATIONS AND DATA PROCESSING

2.1. *Chandra Observations*

The new *Chandra* observations (ObsIDs 5826, 5827, 5828, 6186, 7210, 7211, and 7212) were taken at a variety of instrument roll angles from 2005 February to November using the ACIS-I detector (CCDs I0–I3) in very faint (VF) mode to minimize the background. We reprocessed all observations applying the latest charge transfer inefficiency and time-dependent gain calibrations (acisD2000-01-29gain_ctiN0005.fits). We incorporated nonuniformity of the quantum efficiency and the time and spatial dependence of the contamination on the optical blocking filter. We performed the usual filtering by grade, excluded bad/hot pixels and columns, removed cosmic-ray "afterglows," and applied the VF mode filtering. We also reprocessed two faint mode ACIS-S ObsIDs (3717 and 2707) and treated the front- (S2) and back- (S3) illuminated CCDs independently. We compared the images from the VF and faint mode observations to verify that no artifacts were introduced near the bright jet by use of the large 5×5 pixel event regions in VF mode. We examined the data for background flaring and found moderate flaring in ObsIDs 3717 and 2707 (the back-illuminated CCDs only) for which we excluded approximately half the duration. The total effective remaining observation time varied over the field, since the observations were taken at many different roll angles. A typical effective exposure time is ~525 ks. The background files (see Markevitch 2001a, 2001b for details) were processed in exactly the same manner as the observations.
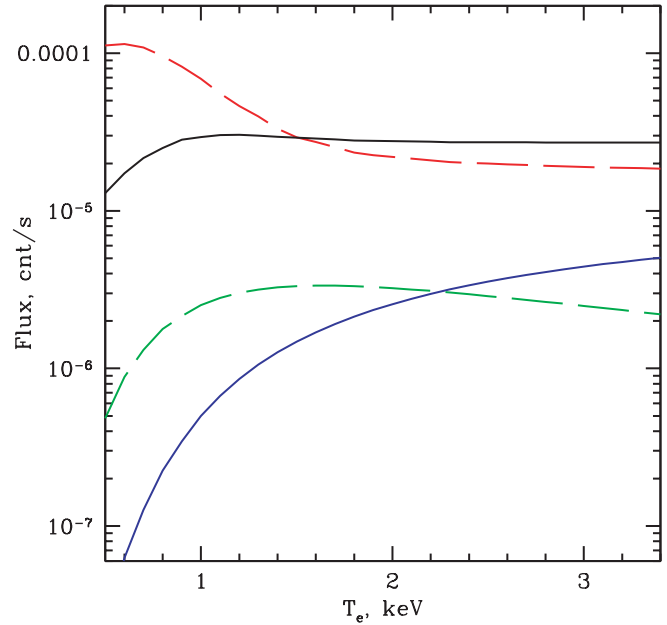

Fig. 1.— Emissivity of an optically thin plasma as a function of temperature as observed by the *Chandra* ACIS-I detector (in units of counts s^{-1} with arbitrary normalization). For the 0.5–1.0 keV soft band (*upper dashed curve*), the emissivity strongly increases for temperatures below 1 keV. For the 1.2–2.5 keV band (*upper solid curve*), the emissivity is nearly independent of gas temperature for temperatures above ~0.75 keV. Hence, surface brightness maps in this band are maps of $\int n^2 dl$, where n is the electron density and l is the path length. In the 3.5–7.5 keV energy band (*lower solid curve*), the photon flux per unit volume, F, can be expressed as $F \propto p^2 \epsilon(T)/T^2$, where $\epsilon(T)$ is the gas emissivity, p is the pressure, and T is the temperature (see text for details). In the hard 3.5–7.5 keV energy band, $\epsilon(T)/T^2$ (*lower dashed curve*) depends only weakly on T (for temperatures from 1 to 3 keV), and hence, the 3.5–7.5 keV band image is approximately an image of the square of the pressure (projected along the line of sight), i.e., total photon flux $\propto \int p^2 dl$. For this figure, we assumed an abundance of 0.75 of solar. Note that for abundances in the range of 0–1 of solar, only the soft-band curve (*upper dashed curve*) changes qualitatively. It shows no peak at low temperatures.

Images were generated by combining the M87 observations after subtracting background and correcting for exposure (which included all the effects mentioned above). When generating merged images, to exclude the readout stripe from the bright nucleus, we excluded rectangular regions extending from the M87 nucleus to the edge of the ACIS chip for each pointing (since the orientation of the readout stripe varies from pointing to pointing). The backgrounds were normalized by time, and small corrections were made using the counts in the 10–12 keV energy band in each image and corresponding background file. Exposure maps in each energy band were computed separately and included vignetting and detector response appropriate to the observed spectrum, assumed to be emission from thermal gas with the redshift, galactic absorption, and elemental abundance of the Virgo Cluster. For quantitative imaging and spectral analysis we relied on the more recent ACIS-I observations alone.

To investigate the properties of the thermal gas that dominates the Virgo core, we selected three energy bands that provide (1) an image of the soft thermal gas (0.5–1.0 keV), (2) a density map (1.2–2.5 keV), and (3) a pressure map (3.5–7.5 keV). Using the full *Chandra* response, we computed the predicted count rate for a unit volume of gas of unit density for different energy bands as a function of gas temperature (see Fig. 1). For the 0.5–1.0 keV band, Figure 1 (*upper dashed curve*) shows that this energy band (Figs. 2–3) focuses on the soft emission.
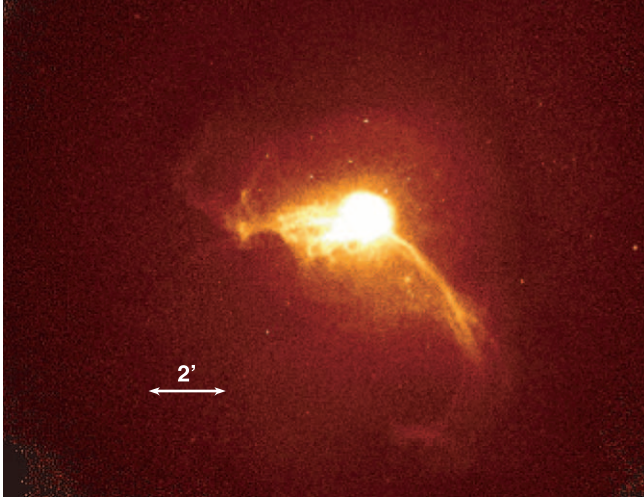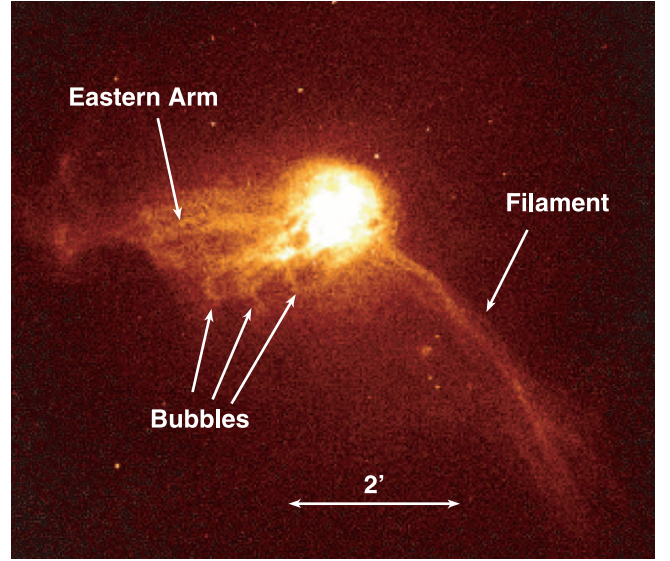
FIG. 2a

FIG. 2b

FIG. 2.—Images of the seven ACIS-I pointings after background subtraction and "flat fielding" in the energy band $0.5-1.0$ keV with 1 pixel = $3''$ at two different scales. (a) The very prominent eastern and southwestern arms (see also Fig. 5, where these are labeled in both the X-ray and radio images). (b) A more detailed view of the tracery of filaments that suggests the similarity between the structures in the eastern and southwestern arms. The long southwestern arm appears to be composed of several intertwined filaments (see location indicated by the label "Filament"). The eastern arm can be interpreted as a series of bubbles (several labeled in right panel) at different evolutionary stages as they rise in the atmosphere of M87. The filamentary structures are very soft and are not apparent at energies above 2 keV (e.g., see Fig. 7).

For the $1.2-2.5$ keV band, Figure 1 (*upper solid curve*) shows that the count rate for a unit volume of unit density is independent of gas temperature, for gas temperatures above about 1 keV. If we express the count rate as

$$C \propto \int n_e^2 \epsilon(T)\,dl, \tag{1}$$

where n_e is the electron density, $\epsilon(T)$ is the volume emissivity of the gas convolved with the *Chandra* response, and l is the path length along the line of sight, the independence of the $1.2-2.5$ keV band emissivity on temperature implies that $C(1.2-2.5 \text{ keV}) \propto \int n_e^2\,dl$. Thus, the $1.2-2.5$ keV band image (Figs. 8a–8b) is a

"density" image (actually the square of the density integrated along the line of sight).

The properties of the $3.5-7.5$ keV band can be determined by rewriting equation (1) using the ideal gas law, $p \propto n_e T$, to eliminate the gas density. We find

$$C \propto \int p^2 \epsilon(T)/T^2\,dl. \tag{2}$$

The lower dashed curve in Figure 1 is $\epsilon(T)/T^2$ for a unit density and unit volume of gas. For gas temperatures from 1 to 3 keV, Figure 1 shows that this expression varies only weakly with temperature. Hence, equation (2) in the hard band can
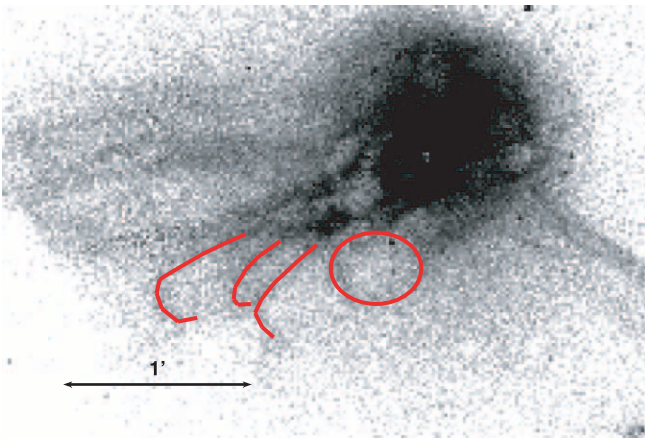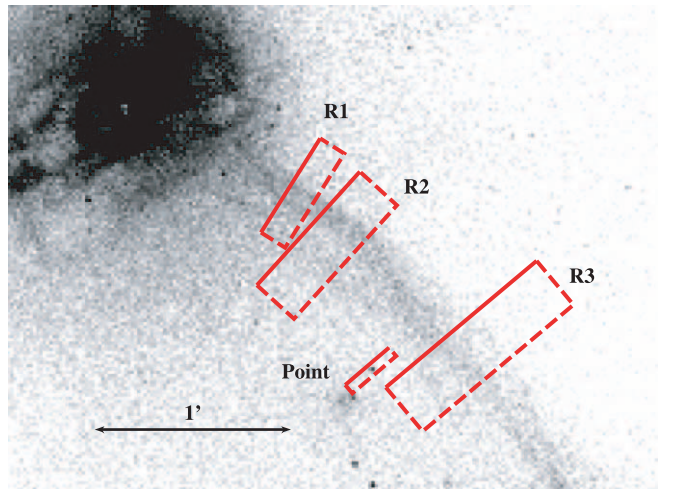

FIG. 3a

FIG. 3b

FIG. 3.—(a) Central region of the $0.5-1.0$ keV band image showing the multiple buoyant bubbles rising in the M87 atmosphere. A series of four "bubbles" are outlined (see Fig. 2b, where the first three bubbles are indicated with arrows). (b) The $0.5-1.0$ keV image of a portion of the southwestern arm indicating the locations of projections and a comparison point source.

be written as $C(3.5-7.5$ keV$) \propto \int p^2 \, dl$. Thus, the hard band (Fig. 7) provides a "pressure" map for the gas (actually the square of the pressure integrated along the line of sight). Hence, bright regions in the hard band indicate pressure enhancements that may be characteristic of shocks. In the analysis and discussion below, we use these three energy bands to investigate the gas around M87.

2.2. *Spitzer Observations*

M87 also was imaged with the Infrared Array Camera (IRAC; Fazio et al. 2004) on the *Spitzer Space Telescope* on 2005 June 11 under Guest Observer Program ID 3228. The exposure time was 300 s for the central region of the galaxy (*Spitzer* data set 0012673792) but only 150 s for a larger region surrounding the target (*Spitzer* data set 0010483200). To create the images in each wave band, the basic calibration data (BCD) were mosaicked using the *Spitzer* Science Center software MOPEX (Makovoz & Khan 2005). Optical distortion was removed in the process, and the images were subpixellated to 0.86″, which is a linear reduction by a factor of $\sqrt{2}$ in each dimension. Figure 6 (*right*), the 4.5 μm image divided by an azimuthally symmetric β-model to remove the strong stellar light gradient, shows the features associated with the jet and counterjet. The synchrotron emission is visually clearest at $\lambda = 4.5$ μm because this bandpass falls between the starlight emission (strongest at 3.6 μm and decreasing with wavelength) and the strong polycyclic aromatic hydrocarbon emission features (which can dominate the 5.8 and 8.0 μm bands).

3. IMAGING RESULTS

Figure 2, the soft-band (0.5–1.0 keV) image (see also Fig. 3), shows that the familiar soft X-ray structures coincident with the radio arms (Fig. 5) are dominated by a filamentary web that extends into a series of bubbles to the south of the eastern arm (Figs. 2b and 3a). The hard-band (3.5–7.5 keV) image, Figure 7 (*left*), shows a shell with the characteristic pressure signature of a weak shock. In addition to these prominent features, the images (see Fig. 5 for an overview of the large-scale structures) show the following:

1. Cavities at the end of the jet that correspond to radio-emitting plasma (seen at 6 cm; see Fig. 6 [*left*], labeled "Counter Jet Cavity" and "Jet Cavity," and compare to 6 cm image in Fig. 6 [*center*] and 4.5 μm *Spitzer* IRAC image in Fig. 6 [*right*]). On the counterjet side, small-scale structures in the radio and IR (Fig. 6 [*center and right*], labeled with arrows) coincide. The counterjet structures probably lie beyond the end of the beamed jet. Shi et al. (2007) found that several of the knots visible in the IRAC images, including the counterjet structures, have spectral indices $f_\nu \propto \nu^{-\alpha}$ with α ranging between 0.7 and 0.9.

2. A very clear demarcation of the counterjet cavity (marked "Counter Jet Rim" in Fig. 6, *left*).

3. An overpressurized egg-shaped region (most likely thermal gas, since there is no corresponding nonthermal radio emission; e.g., see Fig. 6, *center*) of radius $\sim 0.6'$, indicated by the lower arrow in Figure 7 (*right*) and outer (*cyan*) contour in Figure 8b. This overpressurized gas is being driven by the relativistic plasma in the radio cocoon (Fig. 6 [*center*] and magenta contours in Fig. 8b) that has been produced in the current outburst.

4. A rim of soft X-ray emission (see shell labeled "Cool Rim" in Fig. 8b) surrounding the overpressurized gas that represents gas swept up by the expanding "piston" (relativistic plasma of the cocoon).

5. A second, weaker pressure ring at a radius of $\sim 1'$ (indicated by the upper arrow in Fig. 7, *right*) may be the result of a secondary outburst, weaker than that which formed the main 13 kpc shock.

6. The very fine structure of the southwestern arm that may indicate a braided/twisted structure (see region marked "Filament" in Fig. 2 and also Fig. 3b). Although the arm itself is resolved, there appear to be finer filaments suggesting the importance of magnetic fields.

7. A sharp boundary at the southern edge of the eastern arm that does *not* correspond to any radio feature (marked "Edge" in Fig. 5, *left*).

8. A new large X-ray cavity (labeled "Outer Cavity" in Fig. 5, *left*) at a radius of $4.8'-6.2'$ at an azimuth of $\theta = 145°$ lying just beyond the eastern X-ray arms (J2000.0; R.A. = $12^{\mathrm{h}}31^{\mathrm{m}}07.0^{\mathrm{s}}$, decl. = $+12°27'0.0''$). The minimum energy required to inflate the cavity is $\sim 10^{57}$ ergs, and its age (rise time) is about 7×10^7 yr. This feature is coincident with 90 cm radio emission (see Fig. 5 [*right*], the 90 cm radio image).

9. ~ 500 point sources, of which most are LMXBs and ~ 100 are background AGNs (e.g., some are seen in Figs. 2 and 6 [*left*]).

In the following discussion of the new X-ray observation of M87, the intimate relationship between the thermal gas and the relativistic radio-emitting plasma should be kept in mind. Figures 5 and 6 compare the X-ray and radio images and emphasize this complex relationship.

3.1. *The Soft Filamentary Web*

The soft-band image (Figs. 2–3) transforms our X-ray view of M87. With the increased statistics of the longer observation and the focus on the energy band below 1 keV, we see a web of filamentary structures with length-to-width ratios of up to ~ 50. This web is especially pronounced in the eastern arm.

The eastern arm appears to be produced by a series of buoyant bubbles. The youngest is associated with a clearly visible "bud" in the X-ray image (westernmost bubble labeled in Fig. 2, marked "Bud" in Fig. 6 [*left*] and outlined circle in Fig. 3a; see also Forman et al. Figs. 1b–1c). The bud has a radius of 0.9 kpc and is filled with radio plasma (Fig. 6, *left and center*; compare the X-ray and radio images). The minimum energy required to inflate the bud is $\sim 10^{55}$ ergs for a spherical cavity (Forman et al. 2005).

Three bubbles, including the bud, are marked "Bubbles" in Figure 2b, and four are highlighted in Figure 3a. We estimate the rise time of the four features using the approximation in Churazov et al. (2000; their § 3.2) to derive the velocity, v_{rise}, of buoyant bubbles. Equating the buoyancy force to the drag force and taking the galaxy mass from Coté et al. (2001), we find $v_{\mathrm{rise}} \approx 400$ km s^{-1} over the whole inner 40 kpc of M87. With an average separation of the features of approximately 0.5′, the features differ in age by roughly 6×10^6 yr.

The series of bubbles, whose outer rims we only partially see in Figure 3a, may continue into the eastern arm, which shows additional filamentary features. These filaments may be independent buoyant bubbles elongated by the rise of the large buoyant bubble that produced the torus (cap of the column forming the eastern radio arm seen and labeled in Fig. 5, *right*).

The X-ray filamentary structure is likely to be influenced by magnetic filamentation or magnetic flux ropes. We know from Faraday rotation data of the inner radio halo (Owen et al. 1990) and radio emission of the large-scale halo (Owen et al. 2000) that the magnetic fields are highly filamented. The radio filaments are likely magnetic flux ropes. The similarity in scale and geometry
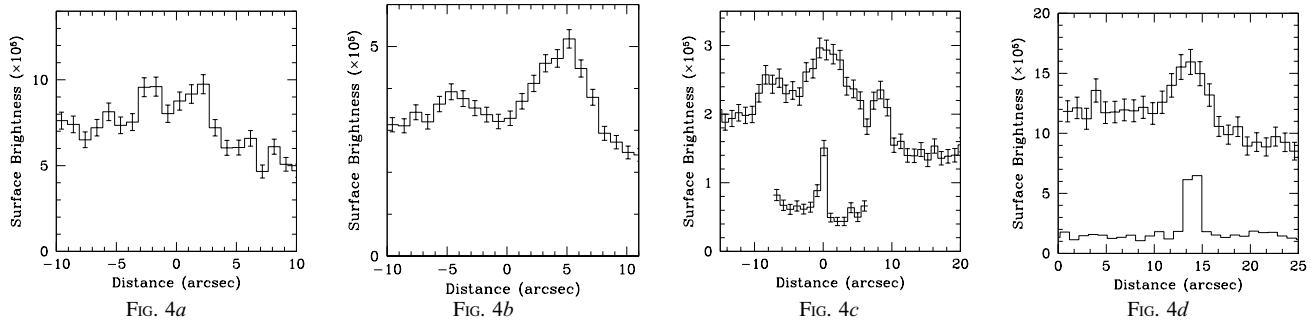
FIG. 4.—The 0.5–1.0 keV projections across the southwestern arm in the regions marked in Fig. 3b. The figures show the complex structure along the arm. (a) This panel (region R1 in Fig. 3b) shows two peaks that may arise either from two separate, close filaments or from the limb-brightened edges of a cylindrical filament. (b) This panel shows (region R2) a continuation of the southwestern arm consisting of two broad filaments. (c) This panel (R3) shows three resolved structures (and a point source below, labeled "Point" in Fig. 3b). Comparison to Fig. 3b shows that the westernmost filament appears to wrap around the central filament. (d) A projection across a boundary of the outer bubble of the series in the eastern arm along with a scaled projection (lower histogram) of a point source 4′ from the nucleus of M87, twice as far as the eastern arm filamentary region.

of the X-ray and radio filaments argues for the importance of magnetic fields in their formation, despite their different emission mechanisms.

The X-ray filaments that form the eastern arm are individually very similar in width to the long, thin X-ray filaments that form the southwestern arm (see Figs. 2, 3, and 5 [left]). Thus, while the eastern arm is significantly broader than the southwestern arm, the structures that compose the eastern arm are individually thin (see Figs. 3a and 4). We have used the marked regions in Figure 3b to extract projections, shown in Figure 4, across the southwestern arm and a point source for comparison. Figure 4a, the projection closest to the center of M87 (R1 in Fig. 3b), shows a resolved arm (broader in extent than a point source) with two subpeaks. These could be either two separate filaments or the limb-brightened edges of a cylindrical tube. Figure 4b shows the onset of a second filamentary structure about 10″ east of the main filament. Figure 4c shows the continuation of the eastern filament, the main filament, and a third filament that in Figure 3 appears to be twisting around the central filament. Comparison of the point-source projections (Figs. 4c–4d) to those of the filaments shows that the filamentary structures have widths (FWHM) of about 4″, 300 pc.

The integrated spectra of the arms are well characterized by a mean temperature of ∼1.5 keV (see Belsole et al. [2001] and the temperature map in Young et al. [2002]). However, Molendi (2002) argued that the spectral data in the arms, on scales as small as 4″ × 4″, require multiple components. This is at least partly caused by the blending of the thin filaments with intrafilament emission. Also, it is likely that the filaments are composed of still finer components that remain unresolved. We will analyze the detailed spectral properties of the arms, using the *Chandra* data, in a later paper.

The *Chandra* observations highlight the differences seen in the structure of the eastern and the southwestern arms. While both arms show long, narrow, spatially resolved filaments, the southwestern arm has only a single set of filaments, while the eastern arm shows multiple sets of filaments and bubbles that increase in scale with distance from the center. In addition, the radio plasma and X-ray thermal plasma are cospatial in the eastern arm, while in the southwestern arm, the X-ray and radio-emitting plasmas avoid each other with the X-ray plasma interior to the surrounding radio plasma (see Fig. 5).

3.2. *Weak Shocks*

The hard-band (3.5–7.5 keV) image, Figure 7 (left), is no less striking than the soft band. We see, for the first time, the un-

ambiguous signature of a shock—a nearly complete ring (indicated by arrows in Fig. 7, left) of higher pressure gas. The outer radius of the hard ring varies slightly as a function of azimuth, θ (measured counterclockwise from west). From the southwest to the northeast ($\theta = -45°$ to $135°$), over nearly $180°$, the outer radius is $R_{outer} = 2.85'$ (13 kpc). In the eastern and southeastern directions ($\theta = 135°-315°$), the outer edge of the ring is slightly smaller, $R_{outer} \sim 2.5'$ (11.5 kpc).

Evidence for two additional features is seen in Figure 7 (right) at radii of $0.6'$ and $\sim 1'$. The region of radius $0.6'$ (outer boundary indicated by the lower arrow) is egg-shaped with the narrower end aligned with the jet (barely visible in Fig. 7, right). This region of high pressure was first reported by Young et al. (2002), who noted a surface brightness "front" at a radius of 40″. This overpressurized region extends to the north, beyond the inner bright radio cocoon seen in the 6 cm radio emission (see Figs. 6 [center] and 8b; see also Hines et al. 1989). We suggest that the plasma in the radio cocoon is the piston that mediates the activity of the central supermassive black hole and drives the pressure waves into the surrounding gas. The $0.6'$ overpressurized region likely arises from the current episode of AGN activity. In an earlier episode of activity, the piston drove the 13 kpc shock. The second weak feature at $\sim 1'$ (5 kpc), indicated by the upper arrow in Figure 7 (right), may be the result of a secondary outburst, weaker than that which produced the primary 13 kpc ring. Both the $0.6'$ and $1'$ features are seen in the surface brightness profiles discussed below.

In our previous study, we detected only the surface brightness enhancement associated with the main 13 kpc shock, but lacked the statistical precision to measure changes in gas temperature. We now detect the increased pressure and spectral hardening characteristic of a weak shock and can measure the temperature increase in the 13 kpc shock. Figure 9a shows the surface brightness profile in the 1.2–2.5 keV (upper curve) and 3.5–7.5 keV (lower curve) energy bands azimuthally averaged over an 80° wedge centered on north where the surface brightness enhancement in the hard band lies at nearly the same radial distance from the M87 nucleus. The most pronounced feature is the shock between 2′ and 3′. Also seen in the profiles is a decrease at 0.6′ (most clearly seen in the hard band between the fourth and fifth bins), which was noted above as being overpressurized gas produced by the present episode of activity (and seen in the hard-band image Fig. 7, right). The second enhancement, possibly a weaker shock, is barely seen at ∼1′.

To derive quantitative parameters of the main 13 kpc shock, we have deprojected the surface brightness profiles. In our analysis

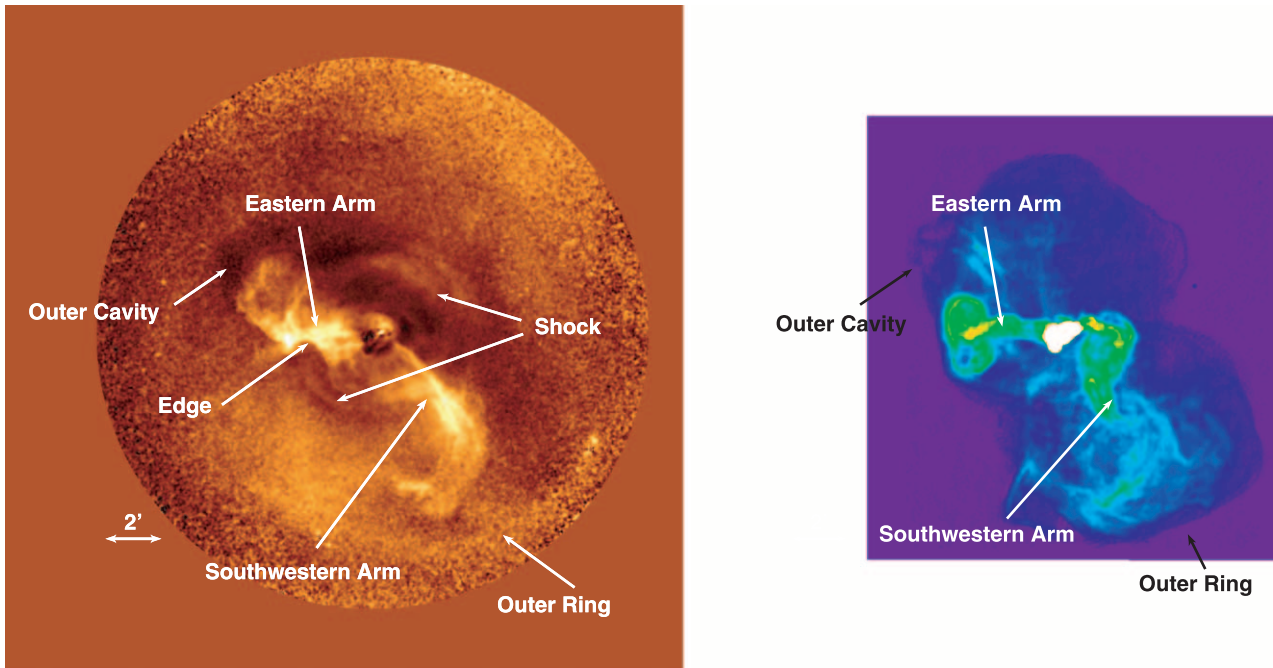Fig. 5.—*Left*: The relative deviations of the surface brightness from a radially averaged surface brightness model, i.e., [data − model]/model over a broad energy band (0.5–2.5 keV). The shock, an outer cavity beyond the eastern arm, a sharp edge in the eastern arm, and an outer partial ring are seen. We have excised the prominent point sources from this image by substituting a local background. *Right*: The 90 cm VLA image from Owen et al. (1990) at the same scale as the *Chandra* image shows the relationship between the X-ray and radio structures. In particular, the eastern and southwestern arms are apparent in both X-ray and radio: the outer X-ray cavity corresponds to an enhancement in the radio, and the outer ring (*enhancement in X-ray image*) lies just beyond the edge of the large-scale radio emission. The radio torus, at the end of the eastern arm, is connected by the arm to the center of M87. The torus and arm produce a "mushroom" shaped structure (*cap and stem*).

we assume spherical symmetry but make no specific assumption about the form of the underlying gravitational potential. We first calculate the surface brightness (in a given energy band) in a set of annuli (or wedges) and choose a corresponding set of spherical shells. The gas parameters are assumed to be uniform inside each shell. Outside $8'$ the emissivity was assumed to decrease with radius as a power law. The projection can then be written as a convolution of the emissivities in each shell with the projection matrix. The solution for emissivities minimizing the χ^2 deviation from the observed surface brightness in the set of annuli can be easily found (see, e.g., Churazov et al. 2003). The emissivities are then converted to electron densities using the *Chandra* spectral response, evaluated for the spectrum with a given temperature and abundance of heavy elements (see the
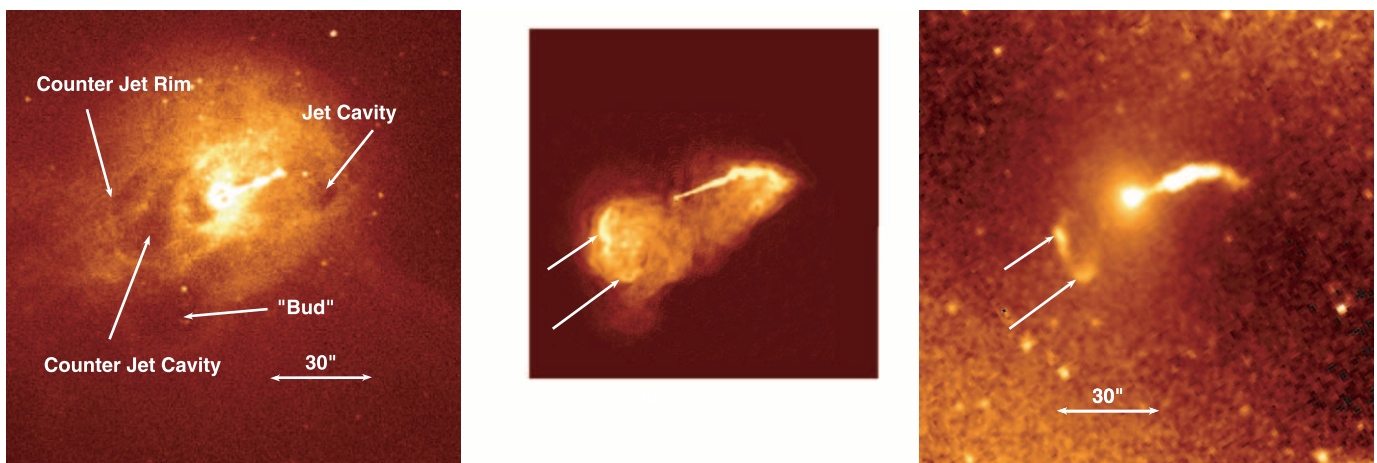

Fig. 6.—*Left*: The 0.5–2.5 keV band full-resolution (1 pixel = 0.492″) image of the entire data set after background subtraction and "flat fielding" of the center of M87. *Center*: The 6 cm VLA radio image from Hines et al. (1989) showing the radio jet and the synchrotron emission from the cocoon. The cocoon of relativistic plasma is the "piston" that mediates outbursts from the central SMBH and drives shocks into the surrounding X-ray-emitting, thermal gas. *Right*: IRAC 4.5 μm image divided by a β-model to remove the strong gradient of emission from the galaxy light. Prominent X-ray features of the central region show the counterjet cavity surrounded by a very fine rim of gas and cavities to the west and southwest of the jet after the jet passes the sonic point and the radio-emitting plasma bends clockwise. The innermost buoyant bubble (X-ray cavity, labeled "Bud" in left panel) coincides with the radio synchrotron emission extending south from the cocoon (*center*). The IRAC image shows the emission from the nucleus and the jet. The IR jet emission ends just before the feature "Jet Cavity" in the X-ray image. On the counterjet side of the nucleus, two bright IR patches (labeled with arrows in the IRAC image) lie within a "C" shaped region. The two bright IR patches coincide with brighter regions of 6 cm emission (also marked with arrows in the center panel) and associated with structures θ and η in Hines et al. (1989). The IR emission (and the coincident radio emission) lie at nearly 90° from the direction of the jet (in projection) and arise from unbeamed emission.
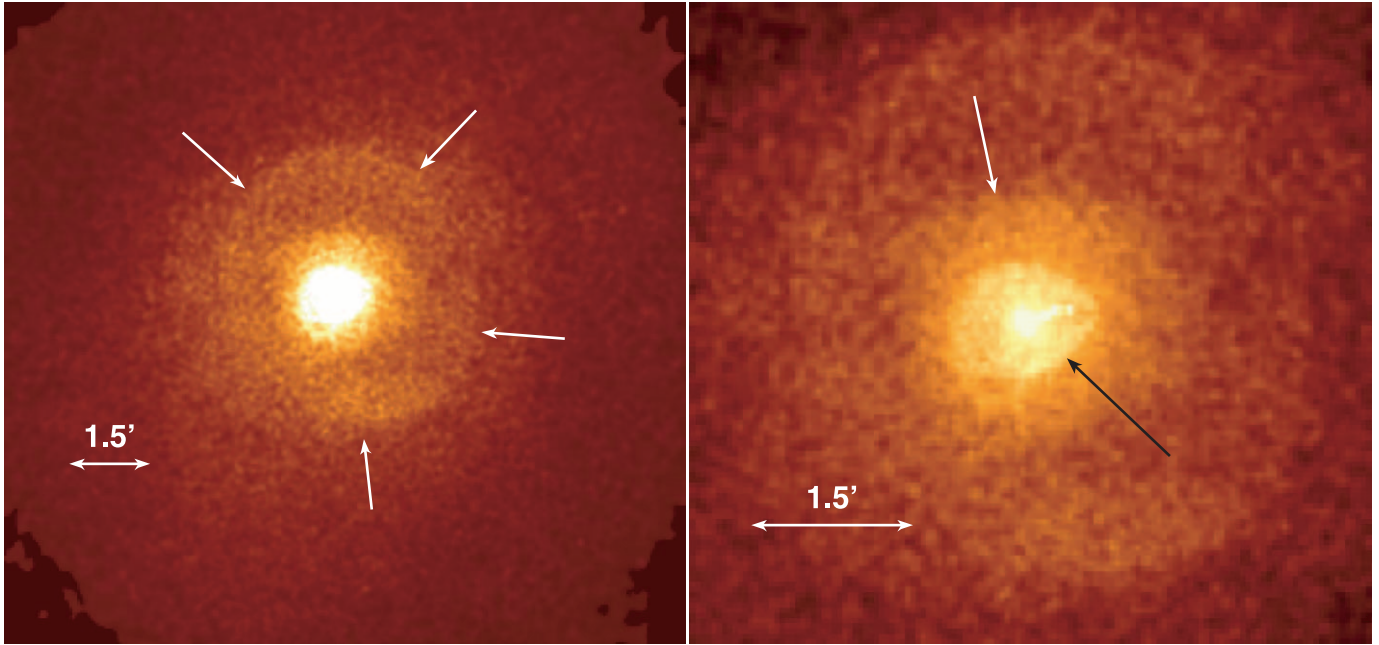
Fig. 7.—Images from the 3.5–7.5 keV energy band at different scales. We have excised the prominent point sources from this image by substituting a local background. *Left*: The 3.5–7.5 keV band image of the seven ACIS-I pointings after background subtraction and "flat fielding." The fine tracery seen in the soft-band image (Fig. 2) is replaced by a nearly azimuthally symmetric ring (*arrows*) of outer radius $\sim2.75'$ (12.8 kpc). As discussed in the text (see also Fig. 1), this hard ring, a map of the square of the pressure projected along the line of sight, is the characteristic signature of a shock driven by an outburst from the central SMBH. *Right*: The central region of the hard-band image showing two additional regions of enhanced pressure. An inner egg-shaped region of radius $\sim0.6'$ (*outer edge, lower arrow*) with the narrow end of the "egg" aligned with the jet (barely visible in the image) was generated during the current AGN outburst from M87's SMBH. An earlier episode of activity is responsible for the 13 kpc shock. A second region of enhanced pressure has an outer edge of $\sim1'$ (*upper arrow*) that may be a weak, secondary shock.

discussion of uncertainties introduced by the assumption of fixed temperature and abundance at the end of this section). The resulting emissivity profiles for the northern wedge are shown in Figure 9b. We note that we are observing a disturbance in the gas that is only approximately spherical. Hence, any shock features are broadened by deviations from spherical symmetry.

We have used the deprojected emissivity profiles in the two energy bands to derive the gas temperature profile. We applied the full *Chandra* response with all telescope and detector effects included (as enumerated above for correcting the exposure maps) to thermal gas models. The resulting temperature profile for the northern wedge is shown in Figure 10. In addition to the surface brightness profiles and deprojection (Figs. 9a–9b) for the northern wedge, we repeated the analysis for the full 360° range of azimuths. The results for both azimuthal ranges, shown in Figure 10, demonstrate a marked rise in the gas temperature at $\sim2.5'$ radius. We note that there is a variation in temperature as a function of azimuth; the northern region (*large circles*) appears slightly hotter than the mean (*small squares*). As we discuss below, despite these differences, the temperature jumps, and hence the derived shock properties (using the Rankine-Hugoniot shock jump conditions), are consistent.

To estimate the magnitude of the temperature rise, we fit the data points in Figure 10 on either side of the shock. For the 360° averaged profile, we consider three data points to be affected by the shock (the peak and the one point on either side), while for the profile to the north, we assume that only two points are affected (the peak and the next point at larger radius; for the northern profile with less data, the uncertainties are larger and the radial range of each bin is larger). The temperature rise is computed from a linear fit to the temperature profile (using three points before the shock and four points beyond) to the peak in each curve. For the two sets of data, the 360° average and the northern wedge, we find $T_{\rm shock}/T_0 = 1.18 \pm 0.03$ and 1.24 ± 0.06, respectively ($T_0 = 1.90 \pm 0.04$ and 1.98 ± 0.04 keV; all uncertainties are statistical only). The temperature jumps, $T_{\rm shock}/T_0$, are consistent and yield a Mach number, $M \approx 1.2$. We have verified that the deprojected hardness ratios yield correct temperatures using direct spectral fits (following the deprojection approach described in David et al. [2001]). However, these detailed temperature fits, although they agree with the deprojection analysis results described above, have unacceptably large values of χ^2, and hence the resulting error bars are difficult to interpret. We defer a detailed discussion of spectral fitting to a later paper, but only note that the best-fit values are in good agreement with those derived from the hardness ratios. Within these limitations, the temperature jump at the shock front is consistent with expectations for the Mach 1.2 shock model of Forman et al. (2005), using the Rankine-Hugoniot jump conditions for a monatomic gas with $\gamma = 5/3$.

We have also analyzed the density jump at the 13 kpc shock to derive an independent estimate of the shock Mach number. Using the azimuthally averaged, deprojected emissivity profile for the 1.2–2.5 keV band (Fig. 9b), we derived the unperturbed density distribution at the location of the shock by fitting a power law to three points before and four points after the shock. The resulting density jump is $\rho_{\rm shock}/\rho_0 \approx 1.33 \pm 0.02$, which yields a Mach number $M = 1.22 \pm 0.02$ (statistical errors only). This independent measurement of the shock strength from the density distribution agrees with that derived from the temperature measurement. *Thus, for the shock at 13 kpc around M87, both density and temperature profiles exhibit the properties of a classical shock in a gas with $\gamma = 5/3$.* The age of the outburst that gave rise to the shock must be approximately the radius of the shock divided by the shock velocity. This age, $t_{\rm outburst} \sim R_{\rm shock}/v_{\rm shock} = 14$ Myr, should slightly overestimate the age of the shock,
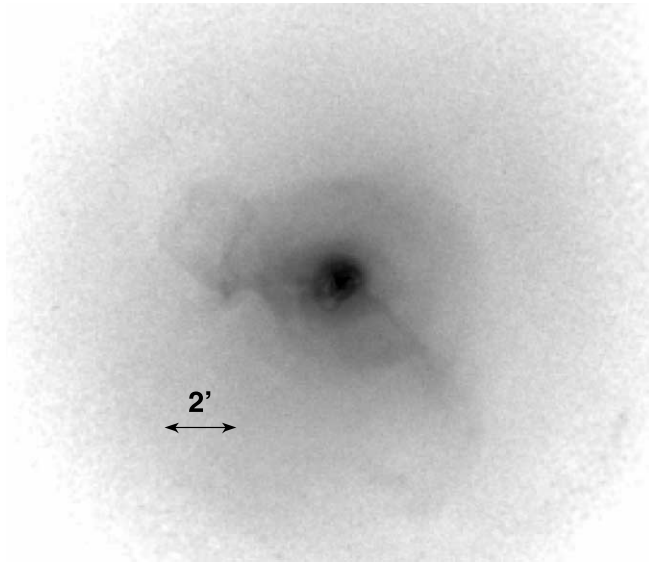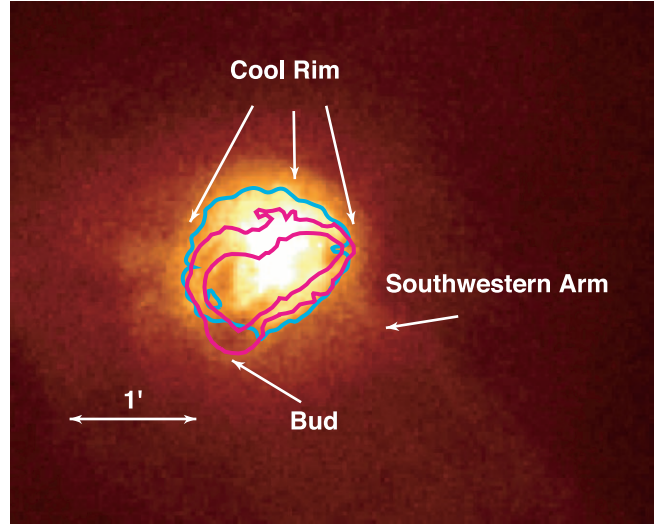
FIG. 8a

FIG. 8b

FIG. 8.—(a) Image from 1.2–2.5 keV derived from seven ACIS-I pointings after background subtraction and "flat fielding." As noted in the text (see also Fig. 1), this image shows the density squared integrated along the line of sight. The pressure shock is seen along with the two prominent arms. Many features, labeled in other images, are seen including the outer cavity, sharp edge, eastern, and southwestern arms labeled in Fig. 5, and the "bud" labeled in Fig. 6. We have excised the prominent point sources from this image by substituting a local background. (b) Central region of the 1.2–2.5 keV band image. The two inner contours (*magenta*) show the 6 cm VLA synchrotron emission, which represents the inner cocoon (the "piston" of relativistic plasma that mediates the energy output of the SMBH and drives the shocks into the atmosphere of M87). This outer contour is derived from the 0.6′ high-pressure region seen in Fig. 7 (*right*) and represents the over-pressurized gas, which is being driven by the piston during the current outburst. The figure shows the cool rim (labeled "Cool Rim") that almost completely sur-rounds the overpressurized region. The cool rim is gas that has been displaced by the piston as it has expanded into M87's atmosphere. Also marked are the bud (arrow denotes its outer cool shell) and the base of the southwestern arm.
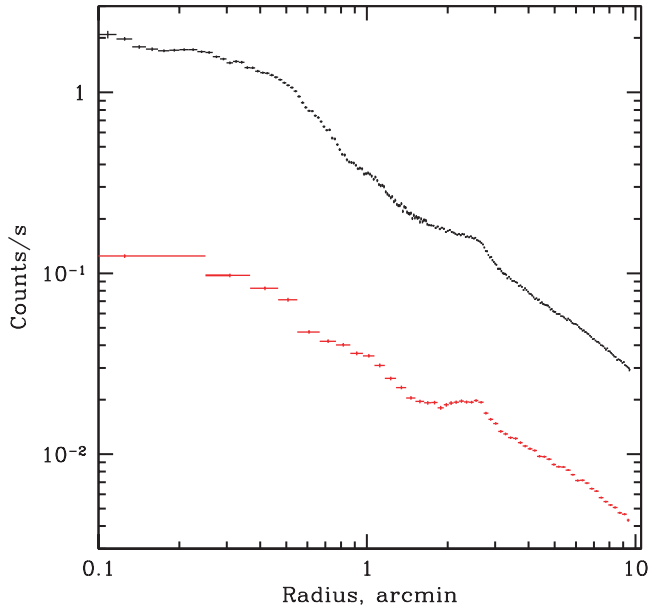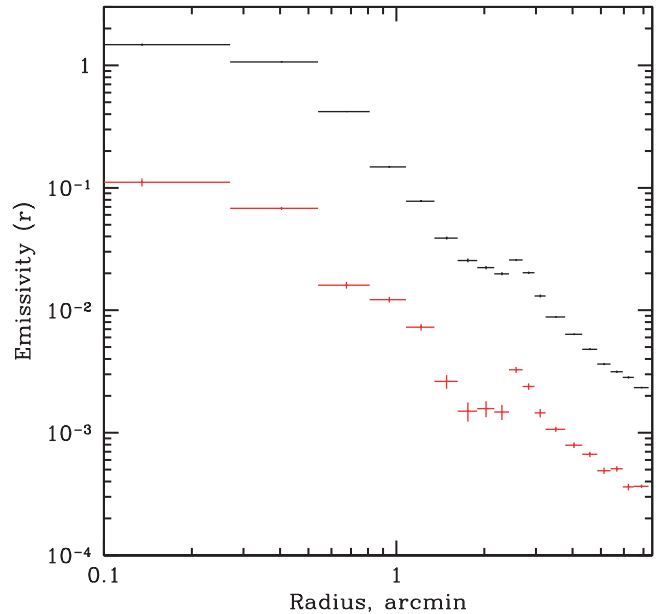

FIG. 9a

FIG. 9b

FIG. 9.—(a) The azimuthally averaged (sector of width 80° centered on north) surface brightness profiles in the 1.2–2.5 keV (*upper curve*) and 3.5–7.5 keV (*lower curve*) bands; these show a sharp edge at ∼0.6′ (most distinctly seen in the hard band as a decrease between the fourth and fifth data points), a moderate flattening of the profile at about 1′, and a strong excess at 2′–3′. (b) The deprojected emissivity profiles, derived from the azimuthally averaged surface brightness profiles in the two energy bands 1.2–2.5 keV (*upper curve*) and 3.5–7.5 keV (*lower curve*). The deprojection shows the very pronounced feature at 2′–3′, which represents the 13 kpc shock. In addition, for a spherical shock one expects a rarefaction region trailing the shock front (e.g., Zel'dovich & Raizer 2002, p. 100) characterized by a density and temperature decrease below the upstream values. Such a rarefaction region is probably seen in Fig. 9b at r ∼ 1.5′–2′, where the emissivity shows a clear depression. The corresponding temperature decrease can also be identified in Fig. 10.
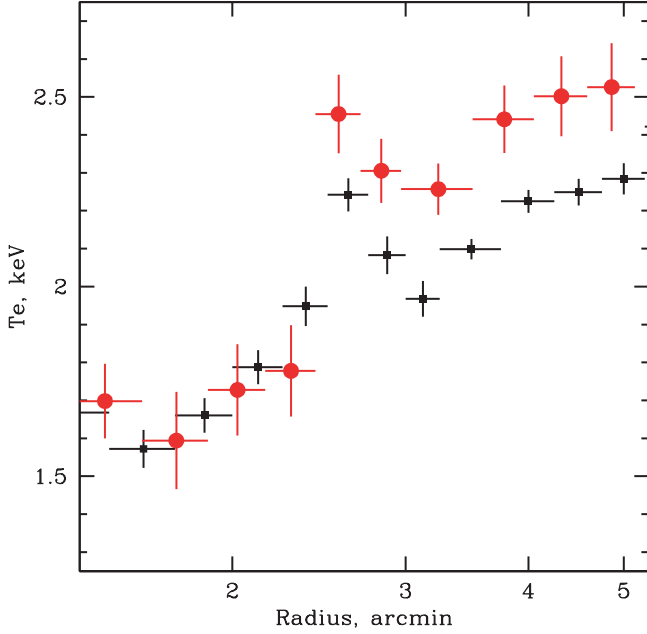
Fig. 10.— Temperature profile derived from the 360° azimuthally averaged data (*small squares*) and the wedge of width 80° (*large circles*) centered on north. We used the deprojected emissivity profiles in the 1.2–2.5 and 3.5–7.5 keV energy bands to derive the gas temperatures. All telescope and detector effects have been included (as enumerated in the text for correcting the exposure maps). There is a clear variation in the temperature as a function of azimuth (the northern region appears hotter), which arises partly from the absence of a perfectly azimuthally symmetric distribution. The temperature rise associated with the shock is apparent in the temperatures derived for both the full 360° average and the northern wedge. We have not computed the temperatures at radii less than 1′ due to the very complex structures seen at smaller radii (see Fig. 6).

since the velocity was higher in the past (see also Forman et al. [2005], who used a simple model to derive an estimate of $t_{\mathrm{outburst}} \sim 11$ Myr).

The gas temperature and densities derived above are subject to systematic uncertainties. We mentioned above that projection and asphericity introduce uncertainties. Projection effects will undoubtedly reduce the temperature peak, while any rarefaction region behind the shock will increase it. While strong shocks can dramatically alter the gas properties behind the shock, the 13 kpc shock in M87 is weak and, hence, behaves almost like an adiabatic wave leaving little disturbance in the gas in the region behind the shock that we use to derive the properties of the shock itself. Also, abundance gradients (see Gastaldello & Molendi [2002] and Matsushita et al. [2003] for detailed discussions of the heavy-element abundance profiles in M87) can affect the radial profiles in different energy bands. The effects on temperature determinations for the bands we have selected are small. Over the temperature range from 1 to 3 keV, abundance variations from 0% to 100% of solar change the temperature by at most ±0.1 keV. We expect any abundance variations to occur gradually as a function of radius (for our azimuthally averaged and deprojected profiles). Furthermore, over the radial range from 1′ to 4′ where we are deriving the temperature and density properties of the shock, the abundance gradients are small (see Matsushita et al. 2003). Detailed spectral fits, where the abundance and temperature are both free parameters, confirm that any effects on the derived temperatures from abundance variations are small. For the gas density, the radial profile would also vary only modestly. For the observed range in abundance in the radial range from 2′ to 3′ (e.g., Molendi & Gastaldello 2001), the

change in the density would be less than 5%. Thus, uncertainties in the shock temperature and density jumps are modest.

4. CONCLUSIONS

M87 and its gaseous halo provide a unique laboratory for investigating the interaction between a SMBH and the surrounding intracluster medium. Because of its low mean temperature of about 2.5 keV, the energy range, 3.5–7.5 keV, where the pressure enhancements of modest shocks are readily observed (Fig. 7), lies within the *Chandra* energy band. Using the 500 ks *Chandra* observation of M87, we find the following:

1. A direct image of a weak shock, a region of enhanced pressure, at a radius of 13 kpc (Fig. 7, *left*).

2. A central overpressurized region (radius 0.6′, seen in the hard-band image Fig. 7, *right*; see also Fig. 8b) that surrounds the piston (radio-emitting relativistic plasma) responsible for mediating the SMBH activity. The 0.6′ overpressurized region is itself surrounded by a cool rim of gas (Fig. 8b). During an earlier phase of activity, the piston drove a shock that we presently observe at 13 kpc.

3. At the shock, gas density and temperature jumps ($\rho_{\mathrm{shock}}/\rho_0 \approx 1.33 \pm 0.02$ and $T_{\mathrm{shock}}/T_0 \approx 1.18 \pm 0.03$, respectively) yield consistent values of the shock Mach number, $M \approx 1.2$, characteristic of a classical shock in a gas with $\gamma = 5/3$.

4. A web of soft filaments that may arise from a series of buoyant bubbles produced by small outbursts from the supermassive black hole at the center of M87. The filaments, the rims of the buoyant bubbles, are resolved by *Chandra* and have widths of approximately 300 pc, although still finer, unresolved structures are likely to exist.

M87 shows a remarkably "organized" and coherent structure in the eastern arm characteristic of a rising buoyant bubble transformed into a torus in both the X-ray and radio images (see Owen et al. 2000 and Churazov et al. 2001) and a second southwestern arm in both radio and X-ray. However, although X-ray cavities are common in cooling core clusters (e.g., Fabian et al. 2000; McNamara et al. 2000; Blanton et al. 2001; Heinz et al. 2002; Mazzotta et al. 2003), the associated thermal gas and radio emission characteristic of a large buoyant bubble (Owen et al. 2000; Churazov et al. 2001; "mushroom shaped" feature) are, so far, only seen in M87.

While progress has been made in understanding galaxy clusters through both *Chandra* and *XMM-Newton* observations, questions remain. The nature of the filaments and importance of magnetic fields in their topology requires additional modeling. Differences between the isothermal "shock" in Perseus (Fabian et al. 2006) and the clear hardening of the shock in M87 need to be understood, and observations of additional clusters are required to place the M87 and Perseus observations in a larger context.

REFERENCES

Begelman, M. 2004, in Coevolution of Black Holes and Galaxies, ed. L. C. Ho (Cambridge: Cambridge Univ. Press), 374
Belsole, E., et al. 2001, A&A, 365, L188
Bertschinger, E., & Meiksin, A. 1986, ApJ, 306, L1
Binney, J., Alouani Bibi, F., & Omma, H. 2007, MNRAS, 377, 142
Birzan, L., Rafferty, D., McNamara, B., Wise, M., & Nulsen, P. 2004, ApJ, 607, 800
Blanton, E. L., Sarazin, C. L., McNamara, B. R., & Wise, M. 2001, ApJ, 558, L15
Böhringer, H., Matsushita, K., Churazov, E., Finoguenov, A., & Ikebe, Y. 2004, A&A, 416, L21
Böhringer, H., Nulsen, P., Braun, R., & Fabian, A. 1995, MNRAS, 274, L67
Böhringer, H., et al. 2001, A&A, 365, L181
Brüggen, M., Kaiser, C., Churazov, E., & Ensslin, T. 2002, MNRAS, 331, 545
Churazov, E., Brüggen, M., Kaiser, C., Böhringer, H., & Forman, W. 2001, ApJ, 554, 261
Churazov, E., Forman, W., Jones, C., & Böhringer, H. 2000, A&A, 356, 788
———. 2003, ApJ, 590, 225
Churazov, E., Sunyaev, R., Forman, W., & Böhringer, H. 2002, MNRAS, 332, 729
Coté, D., et al. 2001, ApJ, 559, 828
David, L., Hughes, J., & Tucker, W. 1992, ApJ, 394, 452
David, L., et al. 2001, ApJ, 557, 546
De Young, D. 2003, MNRAS, 343, 719
Dunn, R., Fabian, A., & Taylor, C. 2005, MNRAS, 364, 1343
Fabian, A. 1994, ARA&A, 32, 277
Fabian, A., Sanders, J., Taylor, G., Allen, S., Crawford, C., Johnstone, R., & Iwasawa, K. 2006, MNRAS, 366, 417
Fabian, A., et al. 2000, MNRAS, 318, L65
Fabricant, D., & Gorenstein, P. 1983, ApJ, 267, 535
Fazio, G. G., et al. 2004, ApJS, 154, 10
Feigelson, E., Wood, P., Schreier, E., Harris, D., & Reid, M. 1987, ApJ, 312, 101
Ford, H., et al. 1994, ApJ, 435, L27
Forman, W., et al. 2005, ApJ, 635, 894
Fujita, Y., Matsumoto, T., & Wada, K. 2004, ApJ, 612, L9
Gaetz, T. 1989, ApJ, 345, 666
Gastaldello, F., & Molendi, S. 2002, ApJ, 572, 160
Gorenstein, P., Fabricant, D., Topka, K., Tucker, W., & Harnden, F. 1977, ApJ, 216, L95
Harms, R. J., et al. 1994, ApJ, 435, L35
Harris, D., Biretta, J., Junor, W., Perlman, E., Sparks, W., & Wilson, A. 2003, ApJ, 586, L41
Heinz, S., Choi, Y., Reynolds, C., & Begelman, M. 2002, ApJ, 569, L79
Heinz, S., & Churazov, E. 2005, ApJ, 634, L141

Hines, D., Eilek, J., & Owen, F. 1989, ApJ, 347, 713
Jordan, A., et al. 2004, ApJ, 613, 279
Kaiser, C., & Binney, J. 2003, MNRAS, 338, 837
Macchetto, F., Marconi, A., Axon, D. J., Capetti, A., Sparks, W., & Crane, P. 1997, ApJ, 489, 579
Makovoz, D., & Khan, I. 2005, in ASP Conf. Ser. 347, Astronomical Data Analysis Software and Systems XIV, ed. P. Shopbell, M. Britton, & R. Ebert (San Francisco: ASP), 81
Markevitch, M. 2001a, *Chandra* Calibration Memo (ACIS; ACIS Background; Cambridge: CXC), http://asc.harvard.edu/cal/
———. 2001b, ACIS Cookbook (Cambridge: CXC), http://cxc.harvard.edu/contrib/maxim/acisbg/COOKBOOK
Marshall, H., Miller, B., Davis, D., Perlman, E., Wise, M., Canizares, C., & Harris, D. 2002, ApJ, 564, 683
Mathews, W., Faltenbacher, A., & Brighenti, F. 2006, ApJ, 638, 659
Matsushita, K., Belsole, E., Finoguenov, A., & Böhringer, H. 2002, A&A, 386, 77
Matsushita, K., Finoguenov, A., & Böhringer, H. 2003, A&A, 401, 443
Mazzotta, P., Edge, A., & Markevitch, M. 2003, ApJ, 596, 190
McNamara, B. R., et al. 2000, ApJ, 534, L135
Molendi, S. 2002, ApJ, 580, 815
Molendi, S., & Gastaldello, F. 2001, A&A, 375, L14
Omma, H., Binney, J., Bryan, G., & Slyz, A. 2004, MNRAS, 348, 1105
Owen, F., Eilek, J., & Kassim, N. 2000, ApJ, 543, 611
Owen, F., Eilek, J., & Keel, W. 1990, ApJ, 362, 449
Perlman, E. S., Biretta, J. A., Sparks, W. B., Macchetto, F. D., & Leahy, J. P. 2001, ApJ, 551, 206
Peterson, J., et al. 2004, in The Riddle of Cooling Flows in Galaxies and Clusters of Galaxies, ed. T. H. Reiprich, J. C. Kempner, & N. Soker (Charlottesville: Univ. Virginia), (astro-ph/0310008), http://www.astro.virginia.edu/coolflow/
Quilis, V., Bower, R., & Balogh, M. 2001, MNRAS, 328, 1091
Reynolds, C., Heinz, S., & Begelman, M. 2001, ApJ, 549, L179
Roychowdhury, S., Ruszkowski, M., & Nath, B. 2005, ApJ, 634, 90
Roychowdhury, S., Ruszkowski, M., Nath, B., & Begelman, M. 2004, ApJ, 615, 681
Ruszkowski, M., Brüggen, M., & Begelman, M. 2004a, ApJ, 611, 158
———. 2004b, ApJ, 615, 675
Shi, Y., Rieke, G., Hines, D., Gordon, K., & Egami, E. 2007, ApJ, 655, 781
Sparks, W. B., Biretta, J. A., & Macchetto, F. 1996, ApJ, 473, 254
Tucker, W., & Rosner, R. 1983, ApJ, 267, 547
Voigt, L., & Fabian, A. 2004, MNRAS, 347, 1130
Young, A., Wilson, A., & Mundell, C. 2002, ApJ, 579, 560
Zakamska, N., & Narayan, R. 2003, ApJ, 582, 162
Zel'dovich, Y. B., & Raizer, Y. P. 2002, Physics of Shock Waves and High-Temperature Hydrodynamic Phenomena (Mineola: Dover)